ASIAN JOURNAL OF CIVIL ENGINEERING (BHRC) VOL. 17, NO. 8(2016)
PAGES 1189-1213

SPECTRAL FINITE ELEMENT SIMULATION OF SEISMIC WAVE PROPAGATION AND FAULT DISLOCATION IN ELASTIC MEDIA

P. Zakian and N. Khaji*
Faculty of Civil and Environmental Engineering, Tarbiat Modares University, P.O. Box 14115–397, Tehran, Iran

Received: 10 March 2016; **Accepted:** 3 June 2016

ABSTRACT

This article employs higher order spectral finite elements to model seismic wave propagation and fault dislocation phenomena in two dimensional elastic media. This study presents two main phases comprising wave propagation and fault dislocation, respectively. In the first phase, accuracy and dispersion assessments are performed to indicate capability of these elements in such problems, revealing suitable polynomial orders which should be utilized for obtaining better accuracy of wave propagation. In the second phase, the split node technique is developed in terms of spectral finite element method in order to simulate both static and dynamic fault dislocations. The split node technique was originally presented for static dislocation using finite element method, whereas it is herein developed to both static and dynamic dislocations using spectral finite element method. Also, the dislocations are modeled in layered half space to incorporate more realistic analyses. Several numerical simulations are provided to demonstrate accuracy and ability of spectral finite elements for modeling of wave propagation and fault dynamics.

Keywords: Wave propagation; fault dislocation; spectral finite element method (SFEM); split node technique (SNT); layered half space; accuracy assessment.

1. INTRODUCTION

Wave propagation phenomenon has been investigated in many fields including ocean waves, seismic waves, electromagnetic waves, sound waves and so on. These phenomena are expressed as partial deferential equations which may have either analytical or numerical solutions. However, analytical solutions only exist for the simple equations under specific initial and boundary conditions. Therefore, although there are problems without successful

*E-mail address of the corresponding author: nkhaji@modares.ac.ir (N. Khaji)

numerical solutions, numerical analysis is of great importance for researchers as they can solve more complex and real-life problems with the least possible limitations. Meanwhile, computational earthquake engineering [1] plays substantial role in applied mathematical modeling of an earthquake. An important issue existing in earthquake engineering is ground response analysis due to seismic waves and earthquake faulting. Earthquake-induced damages of engineering structures are unavoidable, thus for defining and predicting potential seismic loading of a structure, particularly for vital structures, one should calculate site effects including wave propagation, fault movements and soil-structure interaction. Many numerical methods have been applied to wave simulation such as finite difference method (FDM) [2], finite volume method (FVM) [3], finite element method (FEM) [4], boundary element method (BEM) [5], decoupled equation method (DEM) [6, 7], spectral finite element method (SFEM) [8, 9] and physics-based methods [10] among others.

Spectral methods was originally proposed by Patera [11] in computational fluid dynamics, these methods were combined with finite element procedures to overcome complex geometries, apart from their desirable accuracy on dynamic analysis. Nowadays, SFEM is one of the most popular numerical tools for simulation of wave propagation. Komatitsch *et al*. [8, 9] proposed the SFEM for seismic wave propagation and solved wave equations with large-scale domains. Khaji *et al*. [12-14] employed the SFEM for elastodynamic problems and damage detection. Khaji and Zakian [15] developed an efficient stochastic SFEM for uncertainty quantification in elastodynamics. Also, different versions of the SFEM were applied to wave propagation [16-21]: the spectral method, the spectral element method, and the spectral finite element method. It is sometimes hard to find out whether or not a method belongs to one of these kinds [4], and their terminologies are sometimes applied interchangeably as well. Nevertheless, in all cases higher-order polynomials or harmonic functions are usually utilized in the solution space. Since harmonic functions are employed as basis functions and the solutions of wave equations are inherently harmonic functions, the spectral method leads to numerical solutions near to exact solutions. Moreover, some cases mainly deal with frequency domain solutions and are sometimes considered for special problems.

On the other hand, fault dislocation and faulting-induced wave propagation have extensively been performed in the literature. One of the well-known method developed by Melsoh and Raefsky [22, 23] is split node technique (SNT) which was added to the FEM for dislocation modeling without explicit implementation of discontinuities. Even though extended finite element method has recently been applied to earthquake fault modeling [24], SNT-FEM is still a robust and popular approach for these models due to its simplicity, efficiency and minimal limitations as discussed in [25].

In this paper, wave propagation and fault dislocation phenomena will be pursued. The SFEM is used to model these problems and in the case of fault dislocation, static and dynamic dislocations are developed together with the SFEM and the SNT. Accuracy of the SFEM is evaluated for various benchmark examples which illustrate abilities of the proposed SNT-SFEM approach. This is the first combination of the SNT and the SFEM in both static and dynamic statuses. Furthermore, two benchmark examples are considered for wave propagation to investigate parametric aspects of higher order SFEM in such problems.

2. SPECTRAL FINITE ELEMENTS FOR WAVE PROPAGATION

The SFEM is a numerical method collecting features of spectral methods and standard FEM. The SFEM contains approximating polynomials within spectral methods and the spatial discretizing scheme of the FEM. This combination leads to fast convergence of solutions while accuracy of them is enhanced. These features eliminates the restrictions regarding the domain geometry, with significantly lower requirements about numbers of element used in a discretization. Lobatto, Chebyshev, and Laguerre polynomials are usually utilized as approximating polynomials in the SFEM. These polynomials are defined to form a system of non-uniformly distributed nodes whose locations correspond to zeroes of certain polynomials. Thus, the main differences between the FEM and the SFEM may be considered in their interpolation functions and quadrature schemes. Here, Lobatto polynomial and Gauss-Lobatto-Legendre (GLL) are selected as interpolation function and quadrature scheme, respectively. The remaining properties of a SFEM analysis are similar to a standard FEM analysis.

In a spectral finite element, a set of local interpolation functions is defined. Firstly, the degree n_l of the Legendre polynomials has to be selected [15]. Local nodes ($n_l + 1$) of an spectral element are obtained as the roots of the following equation

$$(1-r^2)P'_{n_l-1}(r) = 0 \tag{1}$$

where $P'_n(r)$ expresses the first derivative of the Legendre polynomial of degree *n* defined as a recursive relation of

$$P'_n(r) = \frac{d}{dr} P_{n+1}(r) \tag{2}$$

for which, the following Rodrigues relation implies that

$$P_n(r) = \frac{1}{2^n n!} \frac{d^n}{dr^n} (r^2 - 1)^n . \tag{3}$$

As an algebraic representation, the *k*th derivative of Lobatto polynomial gives

$$P'_k(r) = \frac{1}{2^{k+1}(k+1)!} \frac{d^{k+2}}{dr^{k+2}} (r^2 - 1)^{k+1} \tag{4}$$

The local nodes are also named as the GLL points. The Lagrange interpolating polynomials of order n_l pass through the GLL points. Therefore, a 2D quadrilateral spectral element has $\ell = (n_l + 1)(n_l + 1)$ nodes. Theoretical analyses show that high interpolation accuracy is achieved in this manner. A famous benefit of Lobatto polynomial followed by

the GLL quadrature is diagonal mass matrix in dynamic analysis.

For elastic wave propagation, the following equation governs

$$\rho\ddot{\mathbf{u}} = \nabla\sigma(\mathbf{u}) + \mathbf{f} \quad \text{in} \quad \Omega \tag{5}$$

where $\rho, \sigma, \ddot{\mathbf{u}}, \mathbf{u}$, and $\mathbf{f}$ denote mass density, stress tensor, acceleration, displacement and body force, respectively. Boundary conditions are imposed as follows

Dirichlet (essential) boundary:

$$\mathbf{u} = \mathbf{u}^{\Gamma_D} \quad \text{on} \quad \Gamma_D \tag{6}$$

and Neumann (natural) boundary:

$$\sigma(\mathbf{u}).\mathbf{n} = \mathbf{u}^{\Gamma_N} \quad \text{on} \quad \Gamma_N \tag{7}$$

such that

$$\begin{aligned} \Gamma_D \bigcap \Gamma_N &= \phi \\ \Gamma_D \bigcup \Gamma_N &= \Gamma \end{aligned} \tag{8}$$

and $\mathbf{n}$ is the unit normal vector. Weak form of Eq. (5) with a test function like **w** gives

$$\int_{\Omega} \rho\ddot{\mathbf{u}}\mathbf{w}\, d\Omega = \int_{\Omega} \mathbf{f}\mathbf{w}\, d\Omega - \int_{\Omega} \nabla\mathbf{w}\mathbf{C}\nabla\mathbf{u}\, d\Omega + \int_{\Gamma_N} \mathbf{w}\mathbf{T}\, d\Gamma \tag{9}$$

while the test function belongs to

$$H_0^1(\Omega) = \{w(x) \in [H^1(\Omega)]^{nd}, w = 0 \text{ on } \Gamma_D\} \tag{10}$$

in which $H^1(\Omega)$ and *nd* show Sobolev space and number of dimension, respectively. But in the case of dynamic analysis, the test function belongs to

$$\tilde{H}_0^1(\Omega) = \{w(x,t) \in [H^1(\Omega) \times I]^{nd},\ w(x,t) = g(x,t) \text{ on } \Gamma_D\} \tag{11}$$

with *I* being interval of time variations. Finite dimensional subspace $\tilde{H}_0^h(\Omega)$, so that $\mathbf{u}^h \in \tilde{H}_0^h(\Omega)$, gives

$$\int_{\Omega} \rho \ddot{\mathbf{u}}^h \mathbf{w}^h \, d\Omega = \int_{\Omega} \mathbf{f} \mathbf{w}^h \, d\Omega - \int_{\Omega} \nabla \mathbf{w}^h \mathbf{C} \nabla \mathbf{u}^h \, d\Omega + \int_{\Gamma_N} \mathbf{w}^h \mathbf{T} \, d\Gamma \tag{12}$$

For a 2D domain, the domain is discretized by *ne* elements considering $\Omega \in \Re^2$ and $\sum_{i=1}^{ne} \Omega_i = \Omega$

$$\sum_{i=1}^{ne} \int_{\Omega^i} \rho \ddot{\mathbf{u}}^h \mathbf{w}^h \, d\Omega = \sum_{i=1}^{ne} \left(\int_{\Omega^i} \mathbf{f} \mathbf{w}^h \, d\Omega - \int_{\Omega^i} \nabla \mathbf{w}^h \mathbf{C} \nabla \mathbf{u}^h \, d\Omega + \int_{\Omega^i \cap \Gamma_N} \mathbf{w}^h \mathbf{T} \, d\Gamma \right) \tag{13}$$

Galerkin approach takes the local test function as element interpolation function **H**, that is

$$\mathbf{H} = \begin{bmatrix} H_1 & 0 & H_2 & 0 & \cdots & H_\ell & 0 \\ 0 & H_1 & 0 & H_2 & \cdots & 0 & H_\ell \end{bmatrix}_{2 \times 2\ell} \tag{14}$$

Hence, element matrices are obtained by

$$\mathbf{k}^e = \bar{t} \int_{\Omega^e} \mathbf{B}^T \mathbf{C} \mathbf{B} \, d\Omega \tag{15}$$

$$\mathbf{m}^e = \bar{t} \int_{\Omega^e} \mathbf{H}^T \rho \mathbf{H} \, d\Omega \tag{16}$$

$$\mathbf{f}_b^e = \bar{t} \int_{\Omega^e} \mathbf{H}^T \begin{Bmatrix} f_x \\ f_y \end{Bmatrix} d\Omega \tag{17}$$

$$\mathbf{f}_t^e = \oint_{\Gamma_N} \mathbf{H}^T \begin{Bmatrix} t_x \\ t_y \end{Bmatrix} d\Gamma \tag{18}$$

where $\boldsymbol{\sigma} = \mathbf{C}\boldsymbol{\varepsilon}$, $\boldsymbol{\varepsilon} = \mathbf{B}\mathbf{u}$, $\mathbf{k}^e$, $\mathbf{m}^e$, $\mathbf{f}_b^e$, $\mathbf{f}_t^e$ and $\bar{t}$ represent stress-strain, strain-displacement relationships, stiffness matrix, mass matrix, body force vector, traction force vector and element thickness, respectively. After assembling element matrices and adding concentrated load vector, the following equation of motion is derived as

$$\mathbf{M}\ddot{\mathbf{u}} + \mathbf{K}\mathbf{u} = \mathbf{F} \tag{19}$$

in which $\mathbf{F} = \mathbf{f}_b + \mathbf{f}_t + \mathbf{f}_c$ and a suitable time integration scheme must be employed to solve Eq.(19). Explicit central difference is a suitable one exploiting the diagonal mass matrix. The time step of the dynamic analysis may be taken as

$$dt \le \mathrm{CFL}_{\max} \frac{\min(dx, dy)}{C_L} \tag{20}$$

where dx and dy indicate distance of two nearest adjacent nodes at the x and y directions, respectively; and C_L is velocity of the fastest wave in the domain which is usually interpreted as P (or longitudinal) wave. In addition, $\mathrm{CFL}_{\max}$ implies the maximum CFL (Courant-Friedrichs-Lewy) number depending on the largest period and integration scheme. $\mathrm{CFL}_{\max}$ has been suggested to be less than 0.6 and a value equal to 0.4 may be chosen for considering margin of safety [8, 9].

3. SPECTRAL FINITE ELEMENTS FOR FAULT DISLOCATION

In this section, the SNT is developed for dynamic analysis of spectral finite element models having fault. For complex domains, the problem may not be solved by analytical methods. In this situation, a suitable numerical method is an alternative to solve the problem. The FEM is an appropriate choice for analysis of dislocation when is enriched by the SNT. In the SNT, the FEM or SFEM mesh is constructed to be compatible with the fault (i.e., the dislocation coincides with finite element edges). Elegance and efficiency are what make the SNT popular and desirable. For example, global stiffness matrix is preserved unchanged, but the fault's effects are appeared as force vector. Additionally, we prove that mass matrix will also preserved unchanged in dynamic form of the SNT. In the first step of implementing the SNT into the SFEM, one should determine the elements whose nodes are connected to the fault that are *contributing elements*, and the nodes are known as *split nodes*, and this is why they call the method SNT.

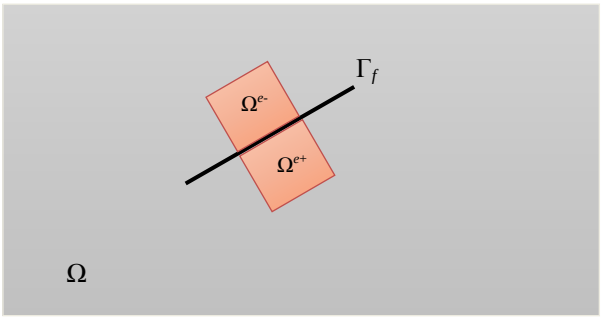

Figure 1. A body consisting of a fault as intersection of contributing elements

Assume a body like Fig. 1 within a fault such that the contributing elements have intersection with the fault at two sides denoted by + (hereafter right side) and – (hereafter left side) sign conventions. Now, one can write equation of motion for each side's contributing element, but two adjacent ones, as follows

For a right contributing element:

$$\begin{bmatrix} \mathbf{m}_{aa}^{e+} & \mathbf{m}_{ab}^{e+} \\ \mathbf{m}_{ba}^{e+} & \mathbf{m}_{bb}^{e+} \end{bmatrix} \begin{bmatrix} \ddot{\mathbf{u}}_{a}^{e+} \\ \ddot{\mathbf{u}}_{b}^{e+} \end{bmatrix} + \begin{bmatrix} \mathbf{k}_{aa}^{e+} & \mathbf{k}_{ab}^{e+} \\ \mathbf{k}_{ba}^{e+} & \mathbf{k}_{bb}^{e+} \end{bmatrix} \begin{bmatrix} \mathbf{u}_{a}^{e+} \\ \mathbf{u}_{b}^{e+} \end{bmatrix} = \begin{bmatrix} \mathbf{f}_{a}^{e+} \\ \mathbf{f}_{b}^{e+} \end{bmatrix} \tag{21}$$

For a left contributing element:

$$\begin{bmatrix} \mathbf{m}_{aa}^{e-} & \mathbf{m}_{ab}^{e-} \\ \mathbf{m}_{ba}^{e-} & \mathbf{m}_{bb}^{e-} \end{bmatrix} \begin{bmatrix} \ddot{\mathbf{u}}_{a}^{e-} \\ \ddot{\mathbf{u}}_{b}^{e-} \end{bmatrix} + \begin{bmatrix} \mathbf{k}_{aa}^{e-} & \mathbf{k}_{ab}^{e-} \\ \mathbf{k}_{ba}^{e-} & \mathbf{k}_{bb}^{e-} \end{bmatrix} \begin{bmatrix} \mathbf{u}_{a}^{e-} \\ \mathbf{u}_{b}^{e-} \end{bmatrix} = \begin{bmatrix} \mathbf{f}_{a}^{e-} \\ \mathbf{f}_{b}^{e-} \end{bmatrix} \tag{22}$$

The matrices imparted to the split nodes *a* and non-split nodes *b* of an element. Γ_f is an internal boundary or fault domain. Displacement of each element can be divided to two parts: average and dislocation values as below

$$\begin{aligned} \mathbf{u}^{e-} &= \overline{\mathbf{u}}^{e-} + \Delta\mathbf{u}^{e-}, \\ \mathbf{u}^{e+} &= \overline{\mathbf{u}}^{e+} + \Delta\mathbf{u}^{e+}. \end{aligned} \tag{23}$$

In which $\overline{\mathbf{u}}^{e-} = \overline{\mathbf{u}}^{e+}$ for two adjacent contributing elements in opposite sides, but $\Delta\mathbf{u}^{e-} = -\Delta\mathbf{u}^{e+}$ stands for the imposed dislocation part of these adjacent elements. The main point is their opposite signs, therefore, slip of the right element may have positive values and slip of the left one may have negative values, and vice versa. Pre-defined slip magnitude *s* is imposed as follows

$$\begin{aligned} \Delta\mathbf{u}_{ij}^{e+} &= \begin{cases} s u_f(t)\cos\theta & \text{at } x \text{ direction}; \ \text{on } \Gamma_f \\ s u_f(t)\sin\theta & \text{at } y \text{ direction}; \ \text{on } \Gamma_f \\ 0 & ; \text{otherwise} \end{cases} \\ \Delta\mathbf{u}_{ij}^{e-} &= \begin{cases} -s u_f(t)\cos\theta & \text{at } x \text{ direction}; \ \text{on } \Gamma_f \\ -s u_f(t)\sin\theta & \text{at } y \text{ direction}; \ \text{on } \Gamma_f \\ 0 & ; \text{otherwise} \end{cases} \end{aligned} \tag{24}$$

where $u_f(t)$ is a normalized dislocation history function of the fault such as one suggested by Haskell [26] that is shown in Fig. 2. Also θ is counterclockwise direction angle of the fault with respect to horizontal line.

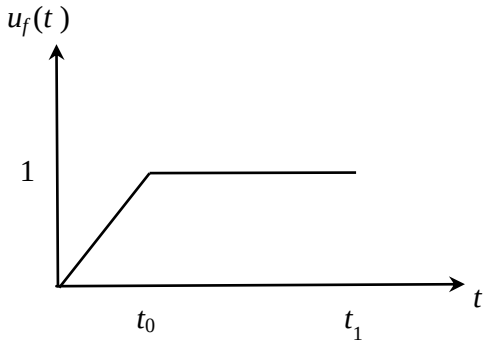

Figure 2. A fault dislocation function

Substituting $\mathbf{u}_a^{e+}=\bar{\mathbf{u}}_a^{e+}+\Delta\mathbf{u}_a^{e+}$, $\mathbf{u}_b^{e+}=\bar{\mathbf{u}}_b^{e+}$, $\mathbf{u}_a^{e-}=\bar{\mathbf{u}}_a^{e-}+\Delta\mathbf{u}_a^{e-}$ and $\mathbf{u}_b^{e-}=\bar{\mathbf{u}}_b^{e-}$ and their second derivatives with respect to time, yields

$$\begin{bmatrix}\mathbf{m}_{aa}^{e+} & \mathbf{m}_{ab}^{e+}\\ \mathbf{m}_{ba}^{e+} & \mathbf{m}_{bb}^{e+}\end{bmatrix}\begin{bmatrix}\ddot{\bar{\mathbf{u}}}_a^{e+}+\Delta\ddot{\mathbf{u}}_a^{e+}\\ \ddot{\bar{\mathbf{u}}}_b^{e+}\end{bmatrix}+\begin{bmatrix}\mathbf{k}_{aa}^{e+} & \mathbf{k}_{ab}^{e+}\\ \mathbf{k}_{ba}^{e+} & \mathbf{k}_{bb}^{e+}\end{bmatrix}\begin{bmatrix}\bar{\mathbf{u}}_a^{e+}+\Delta\mathbf{u}_a^{e+}\\ \bar{\mathbf{u}}_b^{e+}\end{bmatrix}=\begin{bmatrix}\mathbf{f}_a^{e+}\\ \mathbf{f}_b^{e+}\end{bmatrix} \tag{25}$$

and

$$\begin{bmatrix}\mathbf{m}_{aa}^{e-} & \mathbf{m}_{ab}^{e-}\\ \mathbf{m}_{ba}^{e-} & \mathbf{m}_{bb}^{e-}\end{bmatrix}\begin{bmatrix}\ddot{\bar{\mathbf{u}}}_a^{e-}+\Delta\ddot{\mathbf{u}}_a^{e-}\\ \ddot{\bar{\mathbf{u}}}_b^{e-}\end{bmatrix}+\begin{bmatrix}\mathbf{k}_{aa}^{e-} & \mathbf{k}_{ab}^{e-}\\ \mathbf{k}_{ba}^{e-} & \mathbf{k}_{bb}^{e-}\end{bmatrix}\begin{bmatrix}\bar{\mathbf{u}}_a^{e-}+\Delta\mathbf{u}_a^{e-}\\ \bar{\mathbf{u}}_b^{e-}\end{bmatrix}=\begin{bmatrix}\mathbf{f}_a^{e-}\\ \mathbf{f}_b^{e-}\end{bmatrix} \tag{26}$$

Afterwards, we arrive at the following forms

$$\begin{bmatrix}\mathbf{m}_{aa}^{e+} & \mathbf{m}_{ab}^{e+}\\ \mathbf{m}_{ba}^{e+} & \mathbf{m}_{bb}^{e+}\end{bmatrix}\begin{bmatrix}\ddot{\bar{\mathbf{u}}}_a^{e+}\\ \ddot{\bar{\mathbf{u}}}_b^{e+}\end{bmatrix}+\begin{bmatrix}\mathbf{k}_{aa}^{e+} & \mathbf{k}_{ab}^{e+}\\ \mathbf{k}_{ba}^{e+} & \mathbf{k}_{bb}^{e+}\end{bmatrix}\begin{bmatrix}\bar{\mathbf{u}}_a^{e+}\\ \bar{\mathbf{u}}_b^{e+}\end{bmatrix}=\begin{bmatrix}\mathbf{f}_a^{e+}\\ \mathbf{f}_b^{e+}\end{bmatrix}-\begin{bmatrix}\mathbf{m}_{aa}^{e+} & \mathbf{m}_{ab}^{e+}\\ \mathbf{m}_{ba}^{e+} & \mathbf{m}_{bb}^{e+}\end{bmatrix}\begin{bmatrix}\Delta\ddot{\mathbf{u}}_a^{e+}\\ \mathbf{0}\end{bmatrix}-\begin{bmatrix}\mathbf{k}_{aa}^{e+} & \mathbf{k}_{ab}^{e+}\\ \mathbf{k}_{ba}^{e+} & \mathbf{k}_{bb}^{e+}\end{bmatrix}\begin{bmatrix}\Delta\mathbf{u}_a^{e+}\\ \mathbf{0}\end{bmatrix} \tag{27}$$

and

$$\begin{bmatrix}\mathbf{m}_{aa}^{e-} & \mathbf{m}_{ab}^{e-}\\ \mathbf{m}_{ba}^{e-} & \mathbf{m}_{bb}^{e-}\end{bmatrix}\begin{bmatrix}\ddot{\bar{\mathbf{u}}}_a^{e-}\\ \ddot{\bar{\mathbf{u}}}_b^{e-}\end{bmatrix}+\begin{bmatrix}\mathbf{k}_{aa}^{e-} & \mathbf{k}_{ab}^{e-}\\ \mathbf{k}_{ba}^{e-} & \mathbf{k}_{bb}^{e-}\end{bmatrix}\begin{bmatrix}\bar{\mathbf{u}}_a^{e-}\\ \bar{\mathbf{u}}_b^{e-}\end{bmatrix}=\begin{bmatrix}\mathbf{f}_a^{e-}\\ \mathbf{f}_b^{e-}\end{bmatrix}-\begin{bmatrix}\mathbf{m}_{aa}^{e-} & \mathbf{m}_{ab}^{e-}\\ \mathbf{m}_{ba}^{e-} & \mathbf{m}_{bb}^{e-}\end{bmatrix}\begin{bmatrix}\Delta\ddot{\mathbf{u}}_a^{e-}\\ \mathbf{0}\end{bmatrix}-\begin{bmatrix}\mathbf{k}_{aa}^{e-} & \mathbf{k}_{ab}^{e-}\\ \mathbf{k}_{ba}^{e-} & \mathbf{k}_{bb}^{e-}\end{bmatrix}\begin{bmatrix}\Delta\mathbf{u}_a^{e-}\\ \mathbf{0}\end{bmatrix} \tag{28}$$

Clearly, fictitious element force vectors are generated due to the dislocation in terms of element mass and stiffness matrices as derived at right hand side of above equation. These force vectors are hereafter called *dislocation force* vector $\mathbf{f}_d^e$ of an element (a contributing element) as below

$$\mathbf{f}_d^{e+}=-\ddot{u}_f(t)\mathbf{m}^{e+}\boldsymbol{\delta}^{e+}-u_f(t)\mathbf{k}^{e+}\boldsymbol{\delta}^{e+}=-(\ddot{u}_f(t)\mathbf{m}^{e+}+u_f(t)\mathbf{k}^{e+})\boldsymbol{\delta}^{e+} \tag{29}$$

and

$$\mathbf{f}_d^{e-} = -\ddot{u}_f(t)\mathbf{m}^{e-}\boldsymbol{\delta}^{e-} - u_f(t)\mathbf{k}^{e-}\boldsymbol{\delta}^{e-} = -(\ddot{u}_f(t)\mathbf{m}^{e-} + u_f(t)\mathbf{k}^{e-})\boldsymbol{\delta}^{e-} \tag{30}$$

where $\Delta\mathbf{u}^e = u_f(t)\boldsymbol{\delta}^e$ and average displacement values are considered in the assemblage which finally rearranges Eq. (19) as

$$\mathbf{M}\ddot{\mathbf{u}} + \mathbf{K}\mathbf{u} = \mathbf{F} + \mathbf{F}_d \tag{31}$$

in which $\mathbf{F}_d$ illustrates global dislocation vector attained by local dislocation forces in Eqs. (29) and (30). In the static dislocation and in the dynamic dislocation whenever $\ddot{u}_f(t) = 0$, inertial term of dislocation force is eliminated, and hence Eqs. (29) and (30) are degenerated to a dynamic form, that is

$$\mathbf{f}_d^{e+} = -u_f(t)\mathbf{k}^{e+}\boldsymbol{\delta}^{e+} \tag{32}$$

and

$$\mathbf{f}_d^{e-} = -u_f(t)\mathbf{k}^{e-}\boldsymbol{\delta}^{e-} \tag{33}$$

However, we obviously take $u_f(t) = 1$ in a static analysis. Consequently, one can form element-wise dislocation vectors, and then utilize any dislocation history function for dynamic analysis of fault dislocation.

4. NUMERICAL SIMULATIONS

This part presents four numerical simulations using previously mentioned approaches. The first two ones are devoted to benchmark wave scattering problems solved due to Refs. [4, 27]. The remaining ones are two new examples for the proposed SNT-SFEM approach in order to solve fault dislocation in a double layer elastic half space using static and dynamic analyses. All the examples, except for the example 3 which involves a static analysis, are temporally integrated with explicit central difference scheme [28] to utilize the advantageous of diagonal mass matrices. Also, plane strain condition is applied to all the examples. Structured meshes are defined for the examples 1 and 2, while unstructured meshes are considered for the examples 3 and 4. For the unstructured meshes, a suitable ordering algorithm is implemented in order to have a minimal or sub-minimal bandwidth for the matrices. These simulations are entirely programmed in MATLAB.

4.1 Wave propagation in a semi-infinite elastic domain

This problem is also known as a Lamb problem [4] for which domain of this problem is described in Fig. 3. Here, the P-wave velocity, the S-wave velocity and the Rayleigh wave velocity are considered as 3200 m/sec, 1848 m/sec, and 1671 m/sec. The time duration of dynamic analysis is taken as 0.999 sec, such that the P-wave cannot reach the outer boundaries, and hence no absorbing boundary condition is applied. Higher order spectral elements with polynomial degrees of 3, 5, 6 and 8 with 160×80, 96×48, 80×40 and 60×30 meshes are employed, respectively. Therefore, their matrices have the same degrees of freedom providing a fair comparative situation. Two receivers are placed at the surface boundary with distance of 640 m and 1280 m from the loading place, that is a Ricker wavelet line force as below

$$F(x=0,y=0,t)=-10^6(1-2\pi^2 f^2(t-t_0)^2)\exp(-\pi^2 f^2(t-t_0)),\qquad t>0 \tag{34}$$

with central frequency $f=12.5\text{Hz}$ and $t_0=0.1$. Surface displacement recorded by the receivers are depicted in Fig. 4 showing accuracy of 8th order elements, while 3rd and 5th order elements reveal some spurious oscillation impairing solutions. Also, 6th order element can compete against 8th order with much less errors with respect to the lower order elements. Displacement fields at x and y directions, and Von Mises stresses at t=0.982 sec are computed and illustrated in Fig. 5, for the 8th order element which is the most accurate one among others considering identical degrees of freedom.

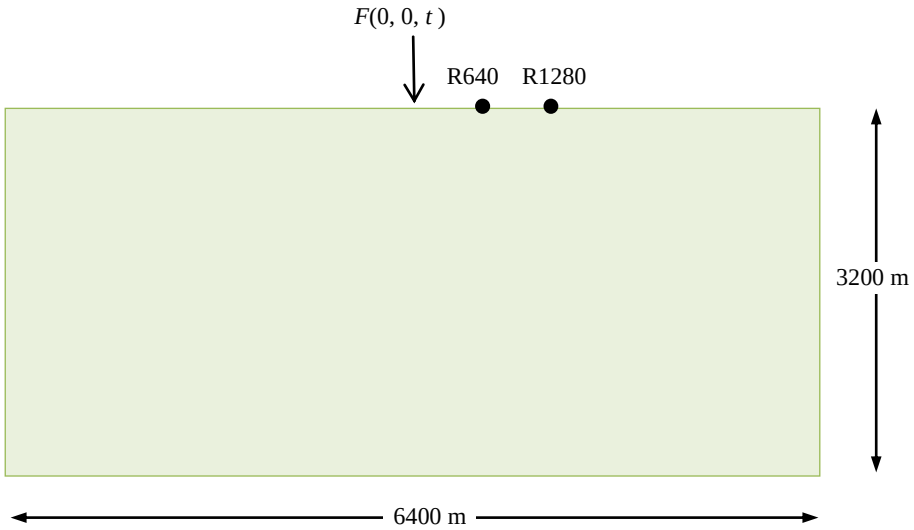

Figure 3. Semi-infinite elastic domain: the prescribed force is placed at the center of surface; R640 and R1280 positions denote receivers' locations at the free surface boundary

4.2 A 2D scalar wave propagation

The scalar wave equation with a Ricker wavelet source at the center of a two-dimensional domain, as per Ref. [27], is given as follows

$$\frac{\partial^2 u}{\partial x^2}+\frac{\partial^2 u}{\partial y^2}+F(0,0,t)=\frac{1}{c^2}\frac{\partial^2 u}{\partial t^2} \tag{35}$$

and

$$F(x=0,y=0,t)=10(1-2\pi^2 f^2(t-t_0)^2)\exp(-\pi^2 f^2(t-t_0)^2), \quad t>0 \tag{36}$$

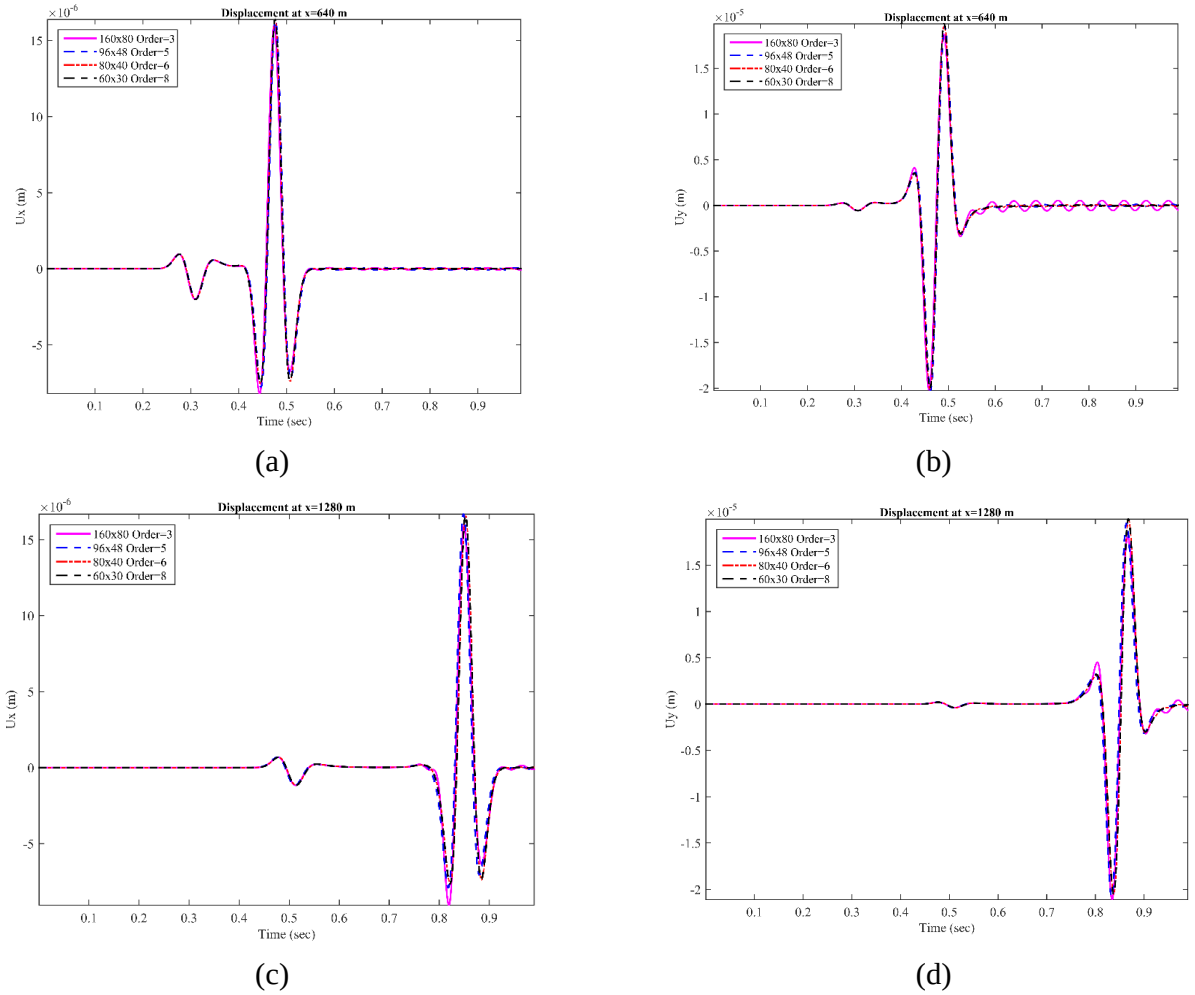

Figure 4. Displacements detected at receivers locations of the free surface boundary: (a) horizontal displacement at R640, (b) vertical displacement at R640, (c) horizontal displacement at R1280, and (d) vertical displacement at R1280

where the wave velocity is $c=1$; central frequency is $f=6\text{Hz}$; $t_0=0.25$; and u is the displacement solution sought. A quarter of the domain [0,1]×[0,1] is analyzed for sake of symmetry. Although absorbing boundary conditions should generally be prescribed at the outer boundary, no absorbing boundary conditions are herein used because for the time duration considered 0.95 sec, the wave does not reach this boundary as same as the previous example. Two meshes 32×32 and 48×48 with polynomial order of 3, and two meshes 12×12 and 18×18 with polynomial order of 8 are generated for this problem which arises the same degrees of freedom for better comparison. Here, 3rd order element has better performance in this problem. However, displacement variations along the x-axis, Fig. 6, and displacement contours, Fig. 7, admit this fact by exhibiting spurious oscillations for different meshes.

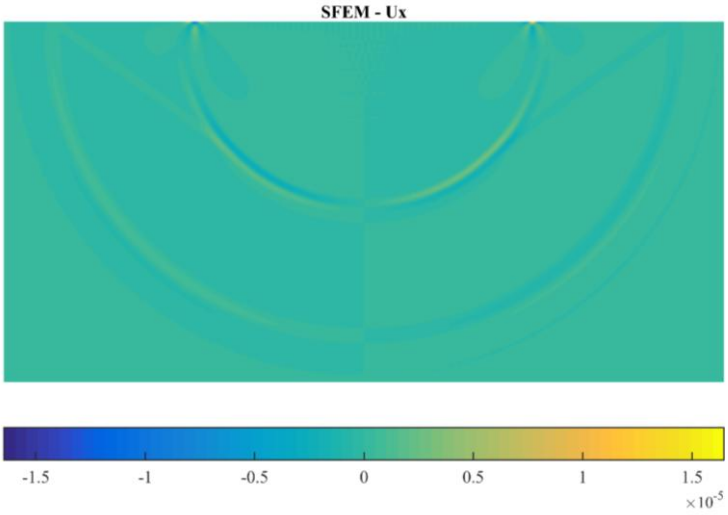

(a)

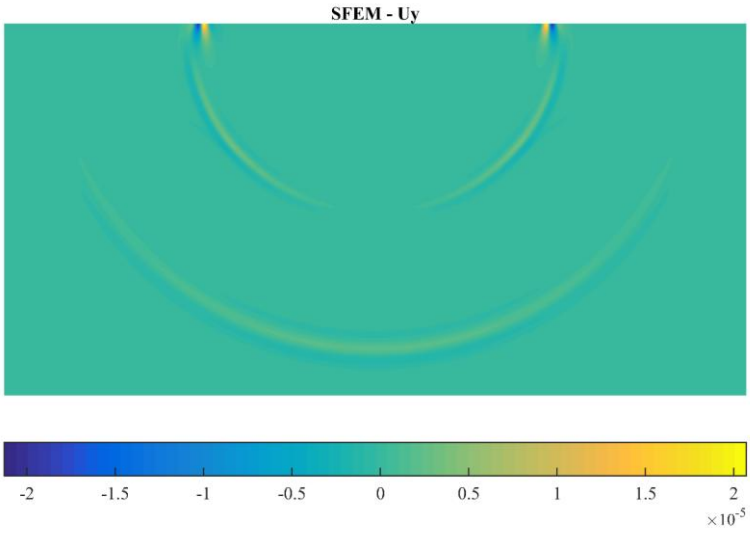

(b)

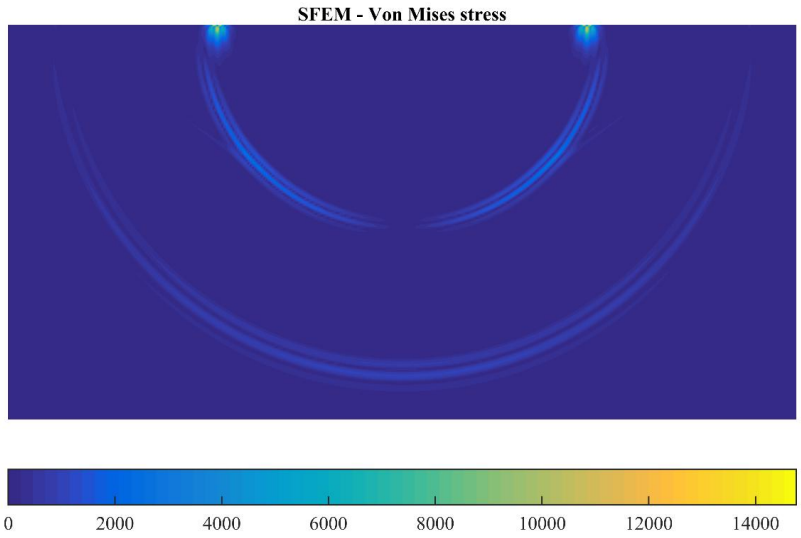

(c)

Figure 5. Response fields: (a) horizontal displacement, (b) vertical displacement, and (c) Von Mises stress

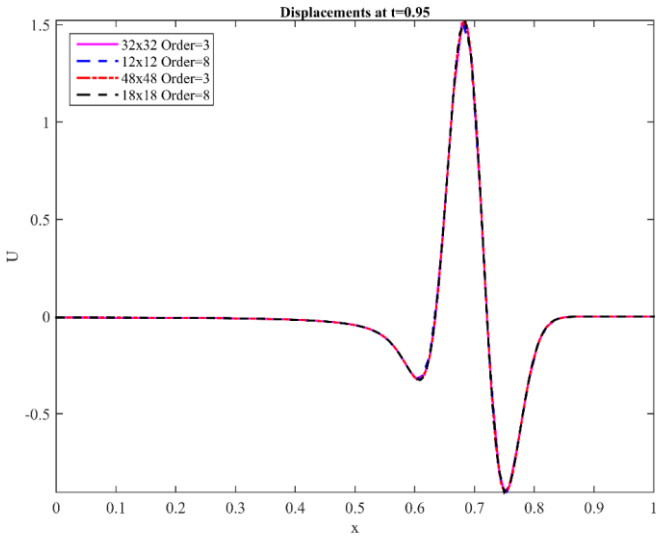

Figure 6. Displacement variations along the x-axis at t=0.95

4.3 Static dislocation of a fault in a layered half space

A double layer elastic half space is indicated in Fig. 8 consisting of an inclined embedded fault shown by red line with 45 degree slope. The fault passes through each layer so that the center of the fault is located at intersection of these layers. Length and slip of the fault are equal to $800\sqrt{2}$ m and 0.8 m, respectively. Layer 1 and layer 2 have different material properties as illustrated. Two unstructured meshes are considered for this problem as

depicted in Fig. 8, the first one consists of 2279 elements, while the second one constitutes 3461 elements. These spectral elements are constructed by the 3rd order polynomial. The main weakness of the SNT is its requirement for mesh alignment around the fault, but this weakness is negligible due to the advantages of the SNT. Here, the meshes 1 and 2 use 10 and 20 segments for discretization of the fault, respectively. Surface displacement responses of the domain at *x* and *y* directions are compared and illustrated in Fig 9. Also, displacement fields of the domain under the fault dislocation at *x* and *y* directions are depicted in Figs. 10 and 11. These figures demonstrate that two meshes give the same trend for responses, indeed, the main and important difference is visible in response values as usual.

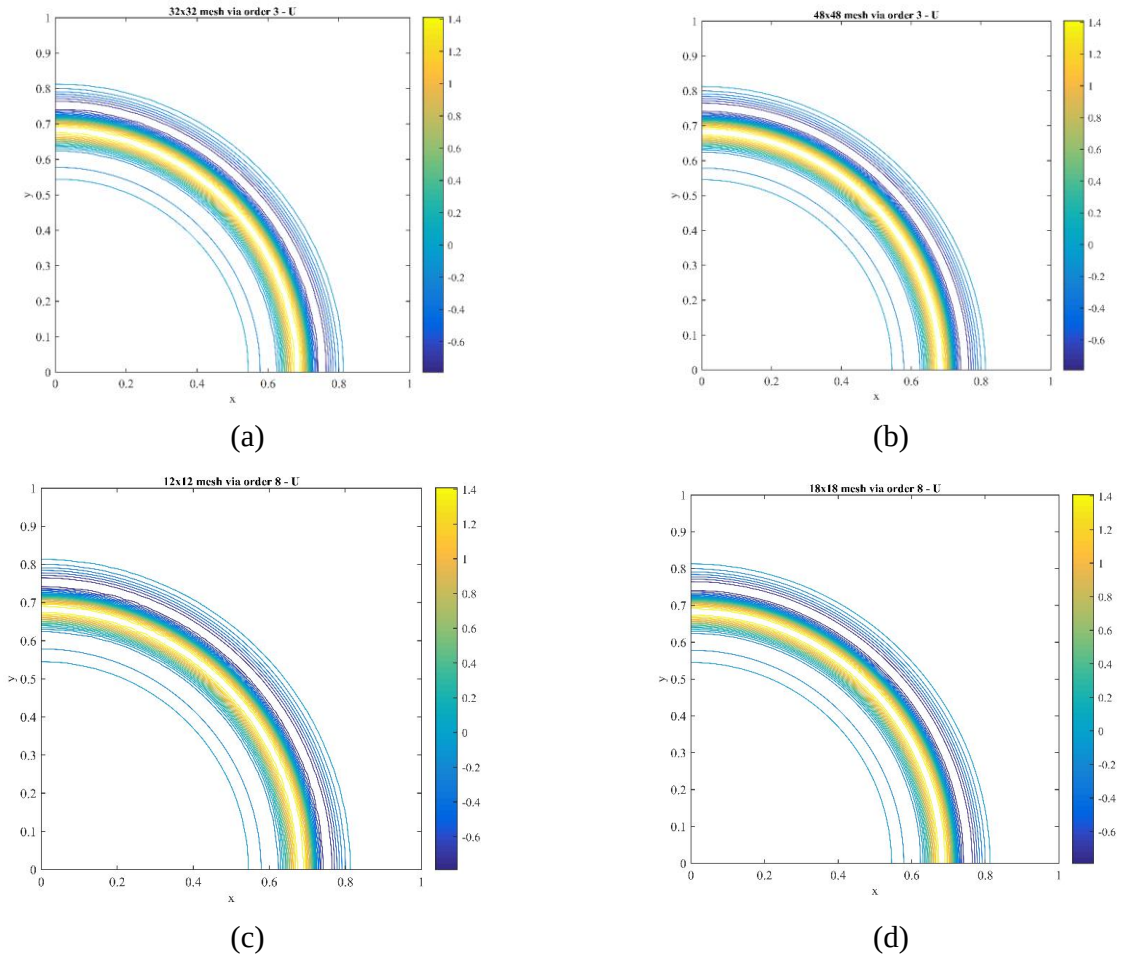

(a) (b)

(c) (d)

Figure 7. Displacement contours at t=0.95: (a) mesh 32×32 with order 3, (b) mesh 48×48 with order 3, (c) mesh 12×12 with order 8, and (d) mesh 18×18 with order 8

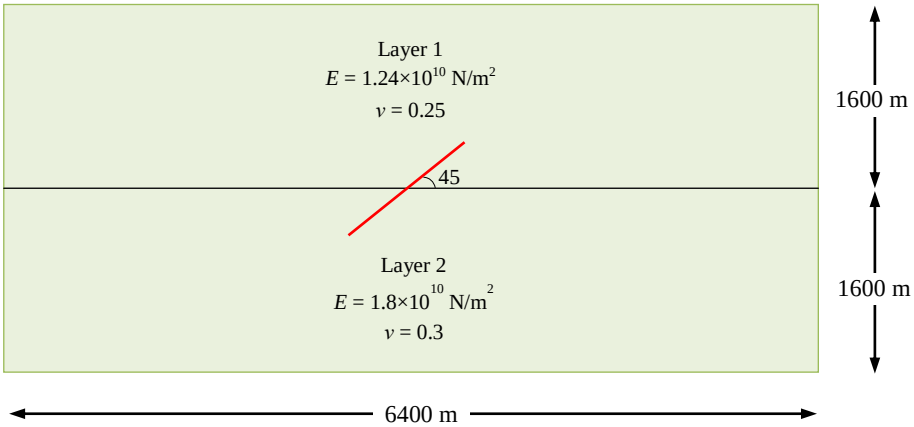

(a)

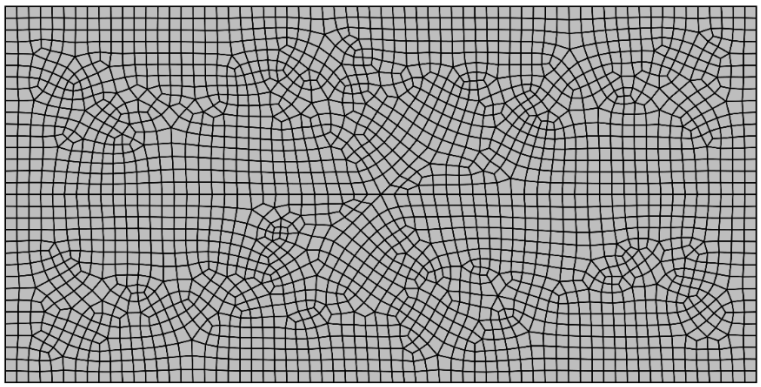

(b)

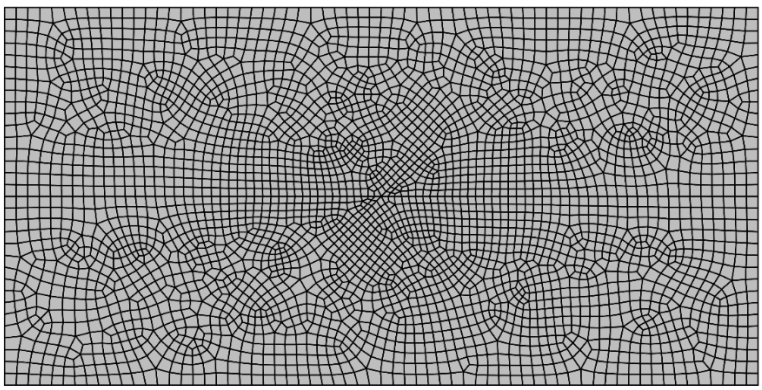

(c)

Figure 8. A double layer domain with a fault and its unstructured meshes: (a) geometry of domain, (b) mesh 1 with 2279 elements, (c) mesh 2 with 3461 elements

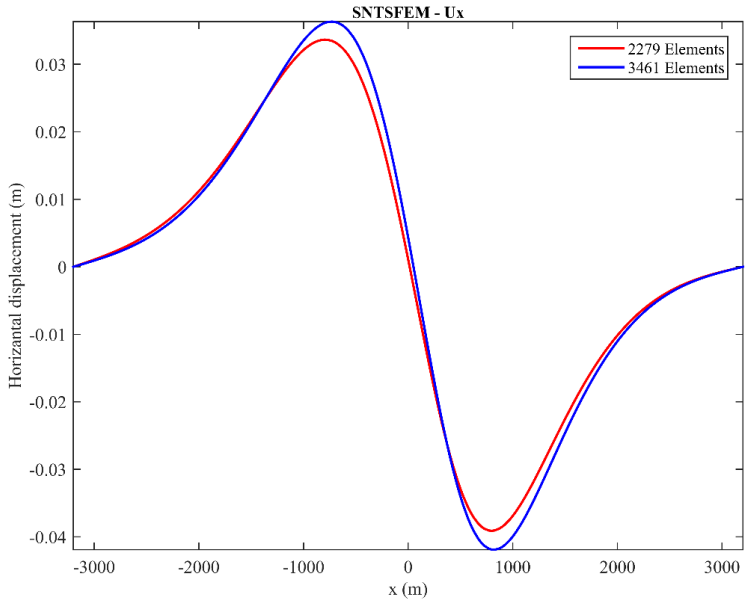

(a)

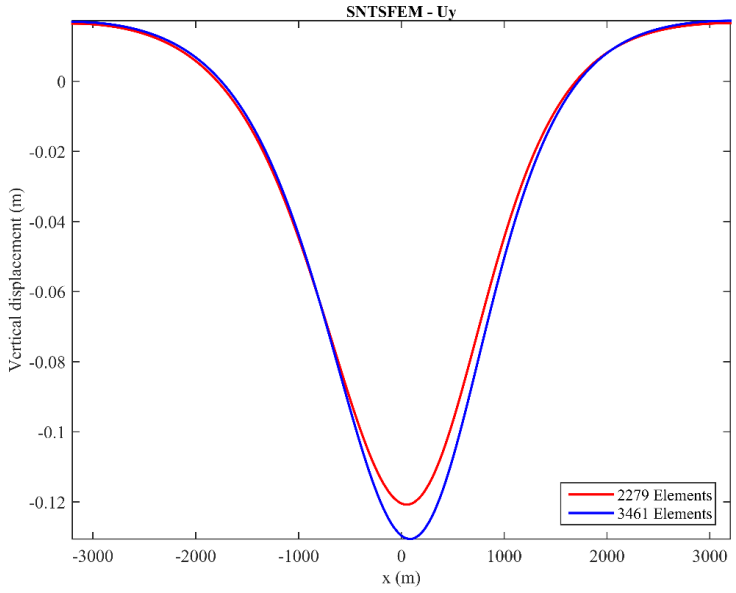

(b)

Figure 9. Surface response of the double layer domain under static dislocation: (a) horizontal displacements, and (b) vertical displacements.

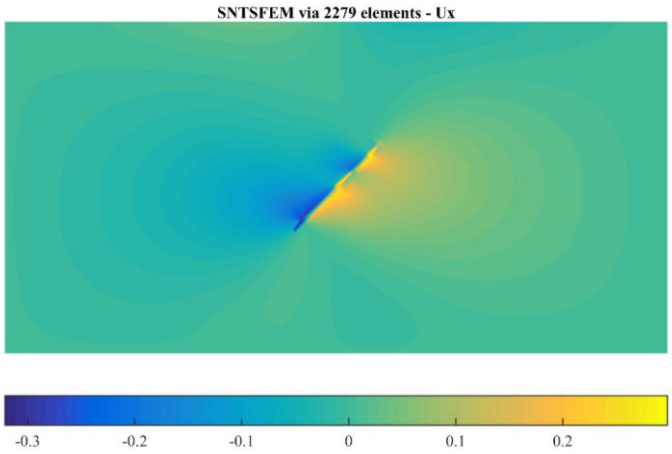

(a)

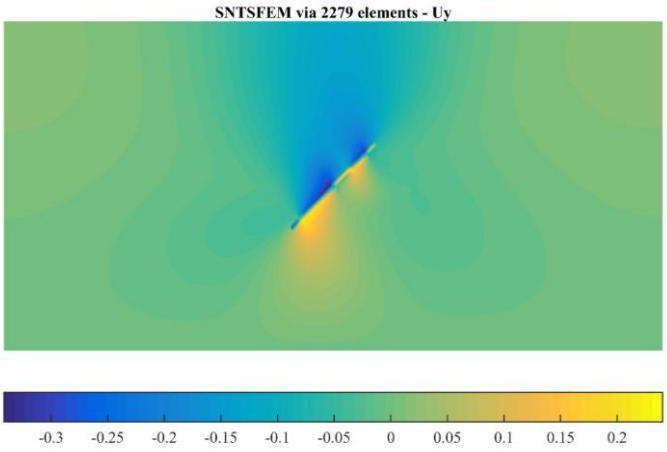

(b)

Figure 10. Response fields due to static fault dislocation simulated by 2279 elements: (a) horizontal displacement, and (b) vertical displacement.

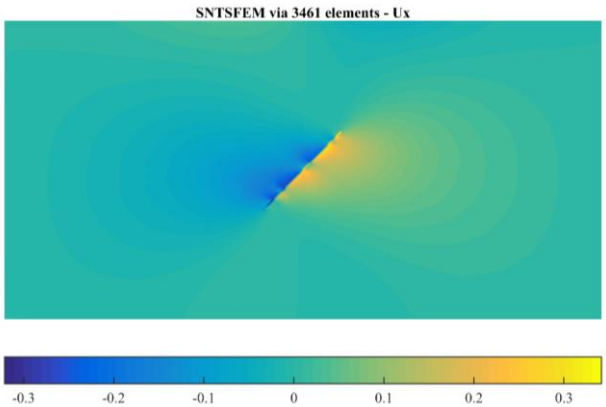

(a)

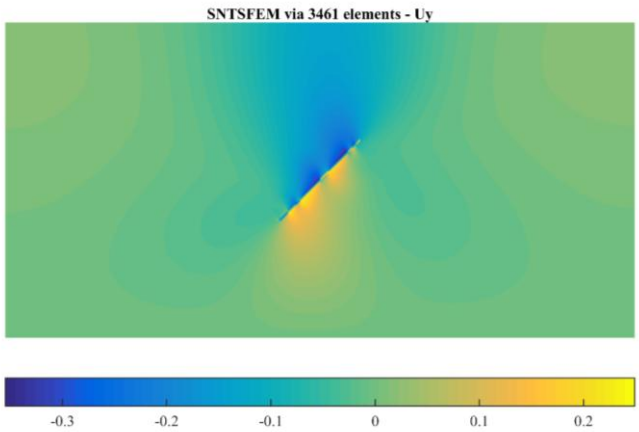

(b)

Figure 11. Response fields due to static fault dislocation simulated by 3461 elements: (a) horizontal displacement, and (b) vertical displacement

4.4 Dynamic dislocation of a fault in a layered half space

This example deals with a problem as same as the example 3, but dynamic form of the previous problem is under consideration here. Thus, a slip dislocation history function is defined as Fig. 2 with t_0, t_1 and s being 0.2 sec, 1 sec and 0.8 m, respectively. The remaining assumptions are identical to the example 3. Surface response histories of this domain at x and y directions are represented in Figs. 12 and 13. Larger number of elements along with finer discretization of the fault creates smoother and more accurate responses in comparison with smaller number of elements. Furthermore, displacement fields of the domain in two time instances at x and y directions are shown by Figs. 14 and 15, these time instances are taken as 0.5 sec and 1 sec, respectively. Faulting-induced wave propagation can be manifested from the results. It should be noted that absorbing boundaries are necessary to be implemented when the traveling waves can reach to boundaries. Nevertheless, absorbing boundaries are not considered here, because the wave cannot reach to boundaries until 1 sec.

5. CONCLUDING REMARKS

In this article, the higher order SFEM is utilized for wave propagation analysis and their accuracy and convergence are investigated. Essential formulations of the SFEM and the SNT-SFEM are presented for wave propagation and further applications in solids and structures. In simple problems, responses of various elements are close together, whereas spurious oscillations and low accuracy are visible in complicated wave problems considering identical degrees of freedom for different meshes composed of various polynomial orders. The numerical assessments show that higher order elements, like 6^{th} and 8^{th} orders, give much better accuracy and minimal dispersion in complicated and large-scale wave problems. Also, the SNT is developed to dynamic and static dislocation simulation

using the SFEM demonstrating desirable accuracy of the SFEM for faulting-induced wave propagation even if distorted mesh is employed. Obviously, a dense mesh with fine part around a fault gives better solutions in sense of accuracy and convergence. Numerical simulations illustrate suitability, ability, accuracy, efficiency and flexibility of the SNT-SFEM as same as the SFEM.

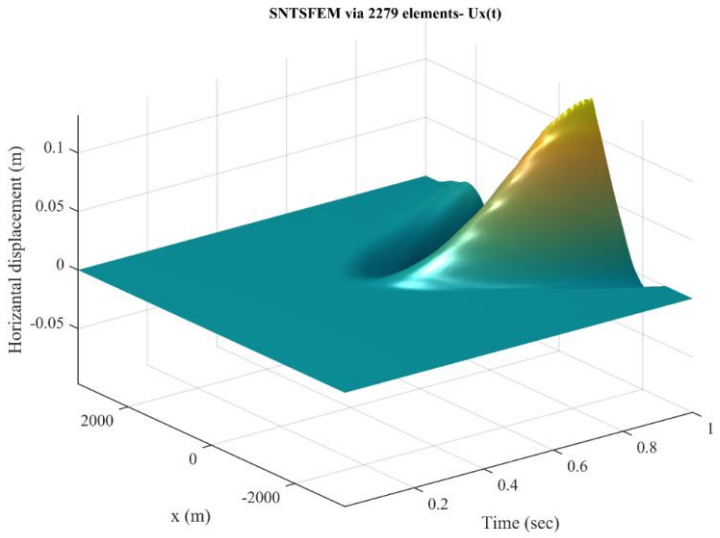

(a)

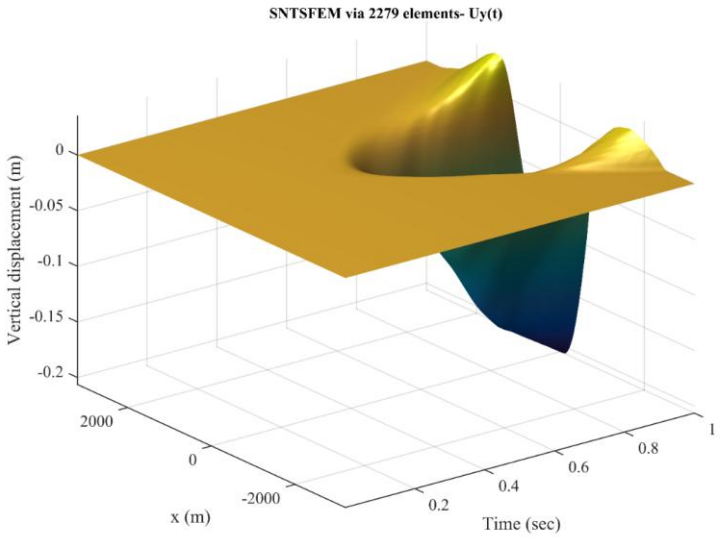

(b)

Figure 12. Surface response of the double layer domain with mesh 1 under dynamic dislocation: (a) horizontal displacements, and (b) vertical displacements

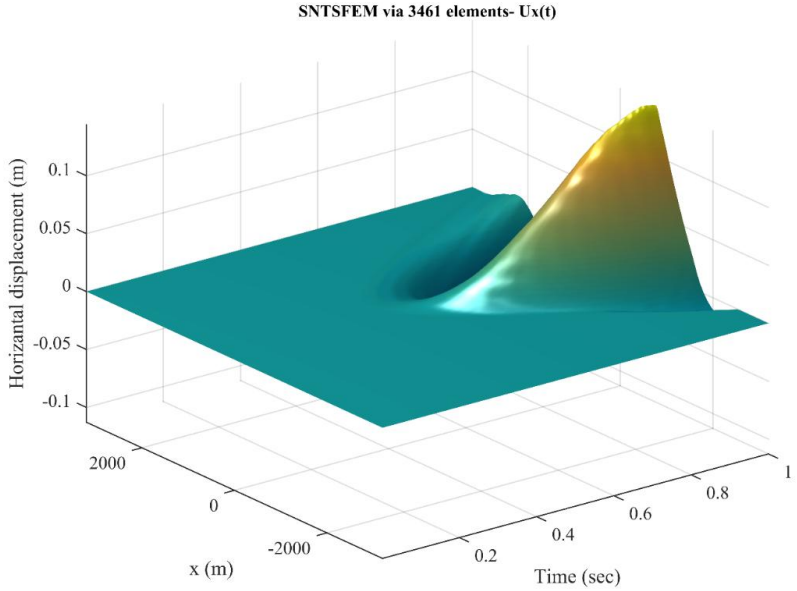

(a)

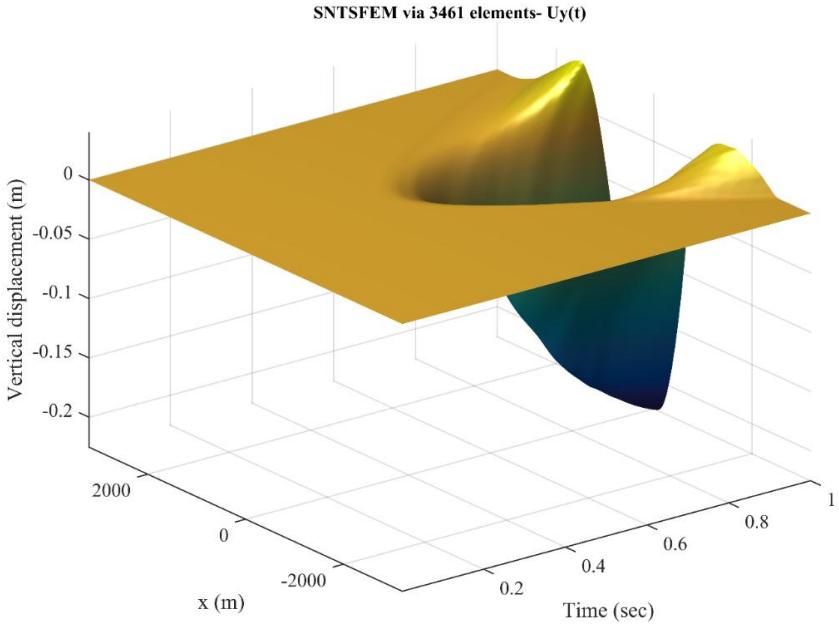

(b)

Figure 13. Surface response of the double layer domain with mesh 2 under dynamic dislocation: (a) horizontal displacements, and (b) vertical displacements

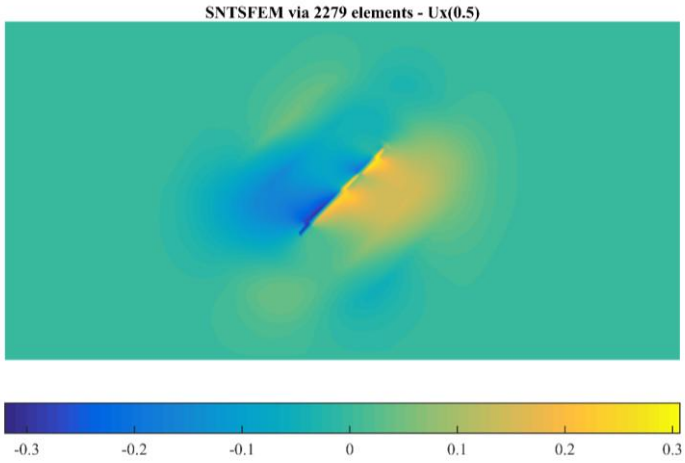
SNTSFEM via 2279 elements - Ux(0.5)
-0.3
-0.2
-0.1
0
0.1
0.2
0.3

(a)

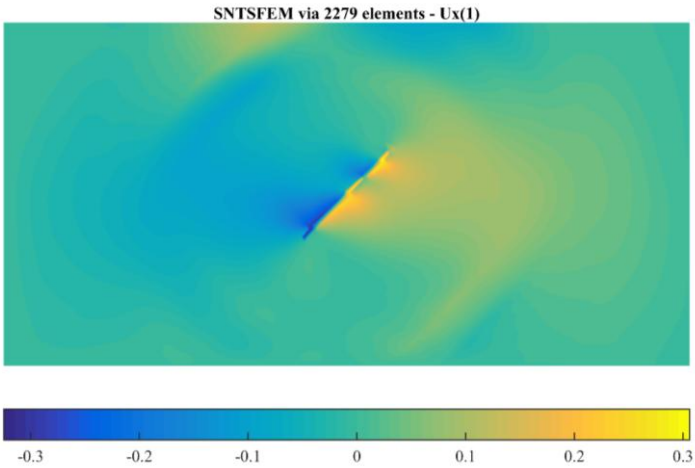
SNTSFEM via 2279 elements - Ux(1)
-0.3
-0.2
-0.1
0
0.1
0.2
0.3

(b)

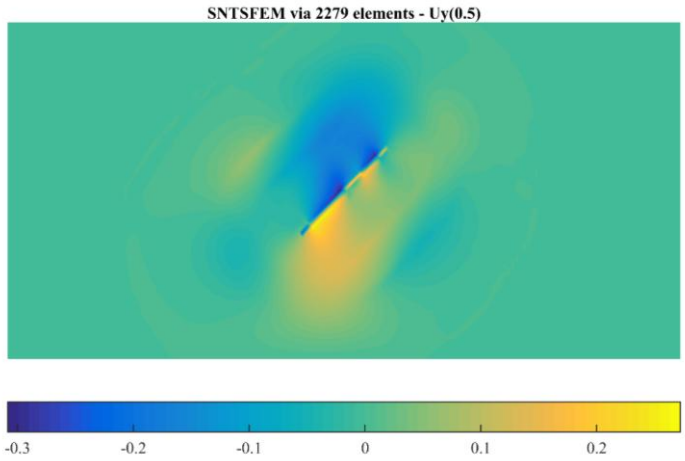
SNTSFEM via 2279 elements - Uy(0.5)
-0.3
-0.2
-0.1
0
0.1
0.2

(c)

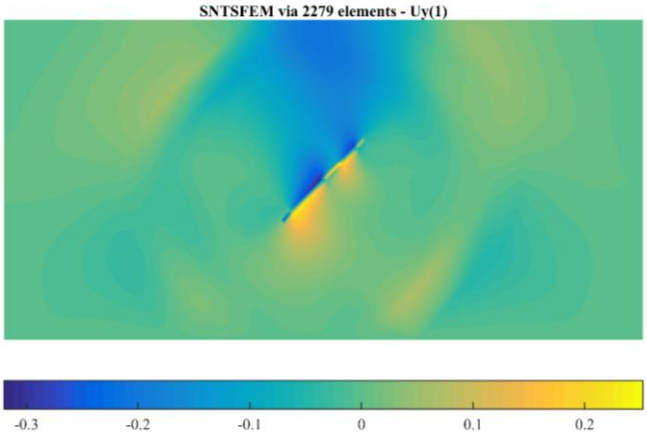

(d)

Figure 14. Response fields due to dynamic fault dislocation simulated by 2279 elements: (a) horizontal displacement at t=0.5 sec, (b) horizontal displacement at t=1 sec, (c) vertical displacement at t=0.5 sec, and (d) vertical displacement at t=1 sec

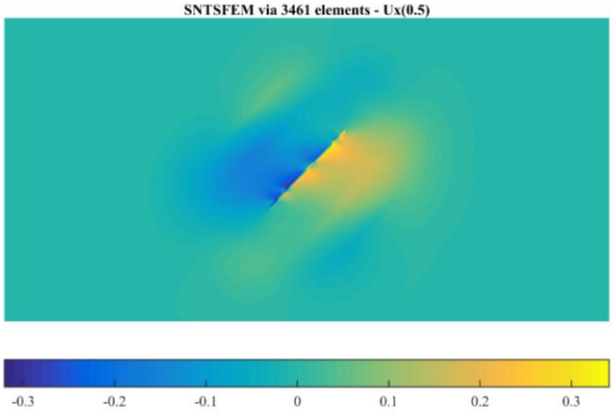

(a)

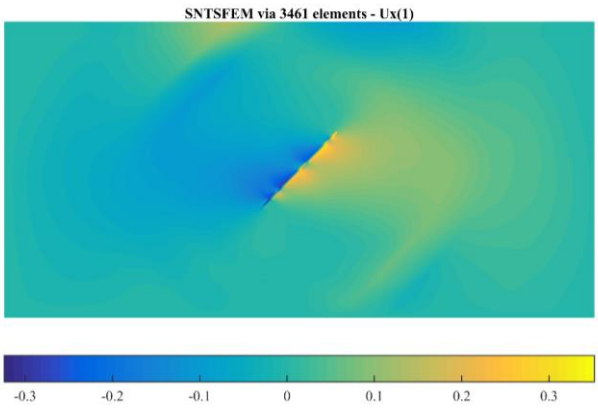

(b)

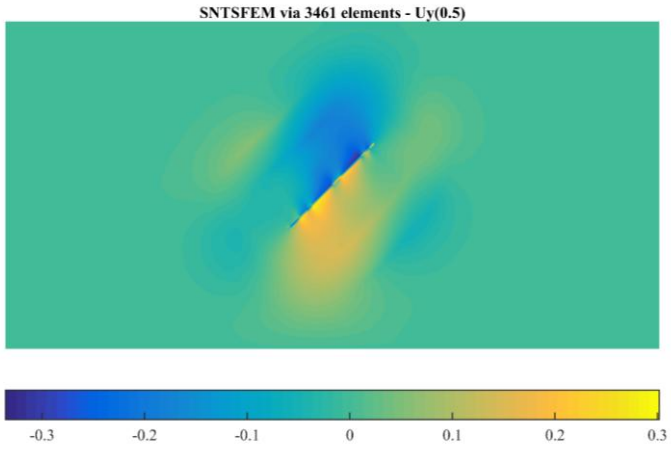

(c)

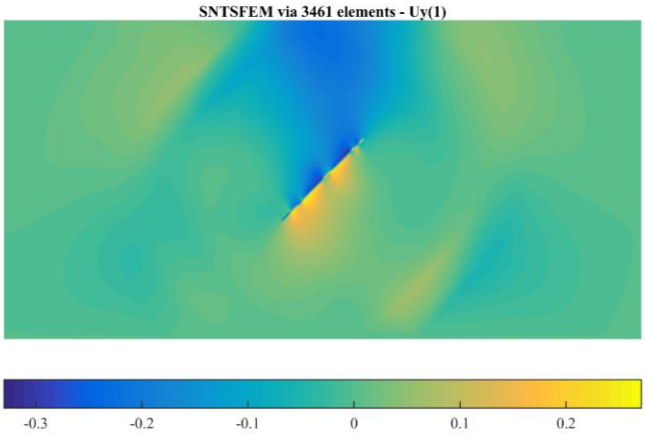

(d)

Figure 15. Response fields due to dynamic fault dislocation simulated by 3461 elements: (a) horizontal displacement at t=0.5 sec, (b) horizontal displacement at t=1 sec, (c) vertical displacement at t=0.5 sec, and (d) vertical displacement at t=1 sec

REFERENCES

1. Hori M. *Introduction to Computational Earthquake Engineering*, World Scientific, 2011.
2. Moczo P, Kristek J, Galis M, Chaljub E, Etienne V. 3-D finite-difference, finite-element, discontinuous-Galerkin and spectral-element schemes analysed for their accuracy with respect to P-wave to S-wave speed ratio, *Geophysical Journal International*, No. 3, **187**(2011) 1645-67.
3. Benjemaa M, Glinsky-Olivier N, Cruz-Atienza VM, Virieux J. 3-D dynamic rupture simulations by a finite volume method, *Geophysical Journal International*, No. 1, **178**(2009) 541-60.

4. Ham S, Bathe KJ. A finite element method enriched for wave propagation problems, *Computers & Structures*, **94-95(**2012) 1-12.
5. Romero A, Tadeu A, Galvín P, António J. 2.5D coupled BEM–FEM used to model fluid and solid scattering wave, *International Journal for Numerical Methods in Engineering*, No. 2, **101**(2015) 148-64.
6. Khodakarami MI, Khaji N. Wave propagation in semi-infinite media with topographical irregularities using Decoupled Equations Method, *Soil Dynamics and Earthquake Engineering*, **65**(2014) 102-12.
7. Khodakarami MI, Khaji N, Ahmadi MT. Modeling transient elastodynamic problems using a novel semi-analytical method yielding decoupled partial differential equations, *Computer Methods in Applied Mechanics and Engineering*, **213-216**(2012) 183-95.
8. Komatitsch D, Tromp J. Introduction to the spectral element method for three-dimensional seismic wave propagation, *Geophysical Journal International*, No. 3, **139**(1999) 806-22.
9. Komatitsch D, Vilotte J-P, Vai R, Castillo-Covarrubias JM, Sánchez-Sesma FJ. The spectral element method for elastic wave equations-application to 2-D and 3-D seismic problems, *International Journal for Numerical Methods in Engineering*, No. 9, **45**(1999) 1139-64.
10. Shafiei M, Khaji N. Simulation of two-dimensional elastodynamic problems using a new adaptive physics-based method, *Meccanica*, No. 6, **49**(2014) 1353-66.
11. Patera AT. A spectral element method for fluid dynamics: Laminar flow in a channel expansion, *Journal of Computational Physics*, No. 3, **54**(1984) 468-88.
12. Khaji N, Habibi M, Mirhashemian P. Modeling transient elastodynamic problems using spectral element method, *Asian Journal of Civil Engineering (BHRC)*, No. 4, **10**(2009) 361-80.
13. Khaji N, Kazemi Noureini H. Detection of a through-thickness crack based on elastic wave scattering in plates, Part I: Forward solution, *Asian Journal of Civil Engineering (BHRC)* No. 3, **13**(2012) 301-18.
14. Kazemi Noureini H, Khaji N. Detection of a through-thickness crack based on elastic wave scattering in plates, Part II: Inverse Solution, *Asian Journal of Civil Engineering (BHRC)*, No. 4, **13**(2012) 431-54.
15. Zakian P, Khaji N. A novel stochastic-spectral finite element method for analysis of elastodynamic problems in the time domain, *Meccanica*, No. 4, **51**(2016) 893-920.
16. Hennings B, Lammering R, Gabbert U. Numerical simulation of wave propagation using spectral finite elements, *CEAS Aeronautical Journal*, No. 1, **4**(2013) 3-10.
17. Kudela P, Krawczuk M, Ostachowicz W. Wave propagation modelling in 1D structures using spectral finite elements, *Journal of Sound and Vibration*, Nos. 1-2, **300**(2007) 88-100.
18. Priolo E, Carcione JM, Seriani G. Numerical simulation of interface waves by high‐order spectral modeling techniques, *The Journal of the Acoustical Society of America*, No. 2, **95**(1994) 681-93.
19. Witkowski W, Rucka M, Chróścielewski J, Wilde K. On some properties of 2D spectral finite elements in problems of wave propagation, *Finite Elements in Analysis and Design*, **55**(2012) 31-41.

20. Żak A, Krawczuk M. Certain numerical issues of wave propagation modelling in rods by the Spectral Finite Element Method, *Finite Elements in Analysis and Design*, No. 9, **47**(2011) 1036-46.
21. Kaneko Y, Ampuero JP, Lapusta N. Spectral-element simulations of long-term fault slip: Effect of low-rigidity layers on earthquake-cycle dynamics, *Journal of Geophysical Research: Solid Earth*, No. B10, **116**(2011) B10313.
22. Melosh HJ, Raefsky A. A simple and efficient method for introducing faults into finite element computations, *Bulletin of the Seismological Society of America*, No. 5, **71**(1981) 1391-400.
23. Melosh HJ, Raefsky A. Anelastic response of the Earth to a dip slip earthquake, *Journal of Geophysical Research: Solid Earth*, B1, **88**(1983) 515-26.
24. Coon ET, Shaw BE, Spiegelman M. A Nitsche-extended finite element method for earthquake rupture on complex fault systems, *Computer Methods in Applied Mechanics and Engineering*, Nos. 41-44, **200**(2011) 2859-70.
25. Van Zwieten GJ, Hanssen RF, Gutiérrez MA. Overview of a range of solution methods for elastic dislocation problems in geophysics, *Journal of Geophysical Research: Solid Earth*, No. 4, **118**(2013) 1721-32.
26. Haskell NA. Elastic displacements in the near-field of a propagating fault, *Bulletin of the Seismological Society of America*, No. 2, **59**(1969) 865-908.
27. Noh G, Bathe K-J. An explicit time integration scheme for the analysis of wave propagations, *Computers & Structures*, **129**(2013) 178-93.
28. Bathe KJ. *Finite Element Procedures*, Prentice Hall, USA, 1996.